

Construction of a novel metal-free heterostructure photocatalyst PRGO/TP-COF for enhanced photocatalytic CO₂ reduction

Yuhan Liu ^a, Yue Wang ^b, Jing Shang ^{a,*}, Jing Peng ^b, Tong Zhu ^a

^a SKL-ESPC & SEPKL-AERM, College of Environmental Sciences and Engineering, and Center for Environment and Health, Peking University, Beijing 100871, PR China

^b Beijing National Laboratory for Molecular Sciences, Radiochemistry and Radiation Chemistry Key Laboratory of Fundamental Science, the Key Laboratory of Polymer Chemistry and Physics of the Ministry of Education, College of Chemistry and Molecular Engineering, Peking University, Beijing 100871, China

ARTICLE INFO

Keywords:

Reduced graphene oxide
Covalent organic frameworks
Carbon dioxide
 $\pi\text{-}\pi$ interaction
S-scheme heterojunction

ABSTRACT

The development of metal-free composite heterojunction catalysts is essential for economical and environmentally friendly carbon dioxide (CO₂) conversion technologies. Most studies neglect the semiconductor property of graphene oxide (GO), which has the potential to participate in the construction of heterojunction catalysts. In this work, a novel organic-inorganic composite metal-free heterojunction photocatalyst was constructed for the photocatalytic CO₂ reduction. Photo-reduced GO (PRGO) and sp²-carbon-chain triazine-based covalent organic framework (TP-COF) can be easily combined and form heterojunctions by a simple and green electrostatic self-assembly method through $\pi\text{-}\pi$ interaction. The photogenerated electrons were transferred from the conduction band of PRGO to the valence band of TP-COF driven by energy band bending and built-in electric field, thus achieving effective charges separation. The strong reductive electrons on this S-scheme heterojunction efficiently and selectively reduced CO₂ to CO. This work provides a new idea for designing GO-based heterojunction photocatalyst PRGO/TP-COF with potential application in CO₂ photoreduction.

1. Introduction

Simulating photosynthesis in nature to achieve photocatalytic reduction of carbon dioxide (CO₂) using water as an electron donor is one of the feasible ways to reach the goal of sustainable carbon cycling and solve the global warming problem [1–3]. An emerging porous polymer material assembled by covalent bonds, covalent organic frameworks (COFs), is considered to be a promising candidate for CO₂ photocatalysis due to the intrinsic properties such as periodic and precise structure, high specific surface area, and customizable functional groups [4–10]. In particular, the enhanced electron delocalization ability of sp²-carbon-linked triazine-based conjugated two-dimensional (2D) COFs offers great possibilities for them in photon absorption and photocatalysis [4,11–14]. In addition, 2D COFs have regular pores and lamellar structures, making them very easy to combine with other 2D materials to form heterogeneous structures [15,16]. Also as a 2D non-metallic material, graphene oxide (GO) has efficient electron transfer capabilities and is often used as a co-catalyst. Currently, a growing number of studies have found that GO is also a semiconductor catalyst with the potential to become a highly available and sustainable standalone photocatalyst [17,18]. However, high carriers

recombination rate and limited light absorption restrict the application of single photocatalyst, and the construction of heterojunction composites is expected to solve these problems to enhance the photocatalytic activity.

Due to the similarity of the carbon skeleton between COFs and GO, the two are likely to interact through strong $\pi\text{-}\pi$ or covalent bonds to form heterojunction composites for accelerated photogenerated carriers separation. Gopalakrishnan et al. [19] prepared covalently bonded rGOx@TpPa-1 photocatalysts to achieve effective reduction of CO₂ to CO in a gas-liquid system (about 200 $\mu\text{mol g}^{-1} \text{ h}^{-1}$ of product yield), but [Co(bpy)³]²⁺ co-catalyst and triethanolamine (TEOA) sacrificial agent were used in the study, and rGO only acted as a co-catalyst. In addition, Yao et al. found that the combination of COF and rGO via $\pi\text{-}\pi$ interactions was more favourable for charges transfer than the covalent bonding, which effectively improved the efficiency of photocatalytic hydrogen production [20,21]. Therefore, the combination of GO and sp²-carbon-conjugated COF through $\pi\text{-}\pi$ interaction is expected to construct photocatalyst with excellent photocatalytic ability. If a metal-free composite photocatalyst based on GO semiconductor properties can efficiently reduce CO₂ without co-catalyst and sacrificial agent, it will have both environmental and economic value, however,

* Corresponding author.

E-mail address: shangjing@pku.edu.cn (J. Shang).



such research has not been reported yet.

In this study, a novel inorganic-organic composite metal-free heterojunction photocatalyst, GO/COF, was constructed and used as a photocatalyst in gas-solid CO₂ reduction system without photosensitiser and sacrificial agent. The strong interaction between GO and COF was found and S-scheme charge transfer pathway was suggested. The GO-based metal-free heterojunction material developed in this study is of importance for CO₂ reduction to useful fuels.

2. Experimental

2.1. Chemicals and materials

Graphene oxide powder was purchased from Times Nano (Chengdu, China) prepared using Hummer's method. 2,4,6-tris(4-formylphenyl)-1,3,5-triazine (TFPT) and 1,4-phenylenediacetonitrile (PDAN) were purchased from Jilin Chinese Academy of Sciences Yanshen Technology Co., Ltd. Cesium carbonate (Cs₂CO₃) was purchased from Konoscience (Beijing, China). 1,4-dioxane and tetrahydrofuran (THF) were purchased from Concord Technology Co., Ltd. (Tianjin, China). Hydrochloric acid (HCl, AR) was purchased from Xilong Scientific Co., Ltd. (China). Ethanol (CH₃CH₂OH, HPLC) was purchased from Thermo Fisher Scientific (China) Co., Ltd. All other reagents were of analytical grade, and were used without further purification.

2.2. Samples synthesis

2.2.1. Preparation of TP-COF

100.7 mg (0.256 mmol) of TFPT and 60.0 mg (0.384 mmol) of PDAN were added in a necked quartz tube, with 248 mg of Cs₂CO₃ as the base catalyst and 5 mL of 1,4-dioxane as the solvent. After dispersing the system ultrasonically for 2 min, three freeze-pump-thaw cycles were conducted, followed by sealing the tube and heating it at 120 °C for 3 days. The precipitate was filtered and separated, soaked and washed with 0.5 mol/L HCl. Subsequently, Soxhlet extraction was performed using THF for 24 h to ensure the removal of unreacted precursors and residual oligomers. The product TP-COF was obtained after dried in vacuum at 120 °C.

2.2.2. Preparation of PRGO

50 mg GO powder was dissolved in 50 mL ethanol/Milli-Q water

mixed solution (V:V=2:1) and sonicated for 1 h. Then 400 μL HCl (5 mol L⁻¹) was added and the solution was sonicated continued for another 1 h. The solution was stirred and irradiated under a 300 W xenon lamp with light intensity of 50 mW/cm² for 1 h. Photo-reduced graphene oxide (PRGO) suspensions were obtained.

2.2.3. Preparation of PRGO/TP-COF composites

50 mg TP-COF powder was dissolved in 50 mL ethanol/Milli-Q water mixed solution (V:V=2:1), and then sonicated for 2 h to obtain a yellow TP-COF suspension. PRGO with the measured Zeta potential of +8.4 mV could be tightly complexed with TP-COF (measured Zeta potential of -31.0 mV) by electrostatic mutual attraction. In the experiment, TP-COF suspension and PRGO suspension were mixed (the total volume of the mixed suspension was 40 mL) and sonicated for 2 h. Then, PRGO/TP-COF composite material was obtained by repeated washing and centrifugation with ethanol and Milli-Q water until the supernatant pH=7, and dried in the oven at 70°C for 10 h. A series of X% PRGO/TP-COF binary hybrid materials with different PRGO load gradients (10%, 15%, 20%, 25%, 30%, 40%, 60%, and 80%) were prepared by changing the mass ratio of PRGO to TP-COF. Fig. 1 shows the synthesis process of X% PRGO/TP-COF nanocomposites.

2.3. Materials characterization

Field-emission scanning electron microscope (FESEM, Merlin Compact, ZEISS Ltd., Germany) and transmission electron microscopy (TEM, JEM-2100 F) was used to observe the morphologies of the photocatalysts. The Energy Dispersive of X-ray Spectroscopy (EDX) was used for qualitative and quantitative analysis of micro-regions of samples. Powder X-ray diffraction (PXRD) data were performed using a Bruker D8 Advance diffractometer with Cu-K α radiation ($\lambda=1.540598\text{Å}$) at 40 kV and 40 mA. Fourier transform infrared spectroscopy (FT-IR) spectra were recorded on a Thermo Scientific Micro Fourier transform infrared spectrometer (Magna-IR750) in the range of 4000–500 cm⁻¹. Raman spectra were obtained by a miniature Raman imaging spectrometer (DXRxi, Thermo Fisher Sci-entific, USA) with laser excitation at 532 nm. X-ray photoelectron spectroscopy (XPS) (Axis Ultra, Kratos Analytical Ltd., UK) was operated at 300 W using a double anode (Mg, Al) target. Ultraviolet photoelectron spectroscopy (UPS) was performed with Thermo EscaLab 250Xi to calculate the work function of the samples. Absorption spectra of GO and PRGO samples were recorded using a

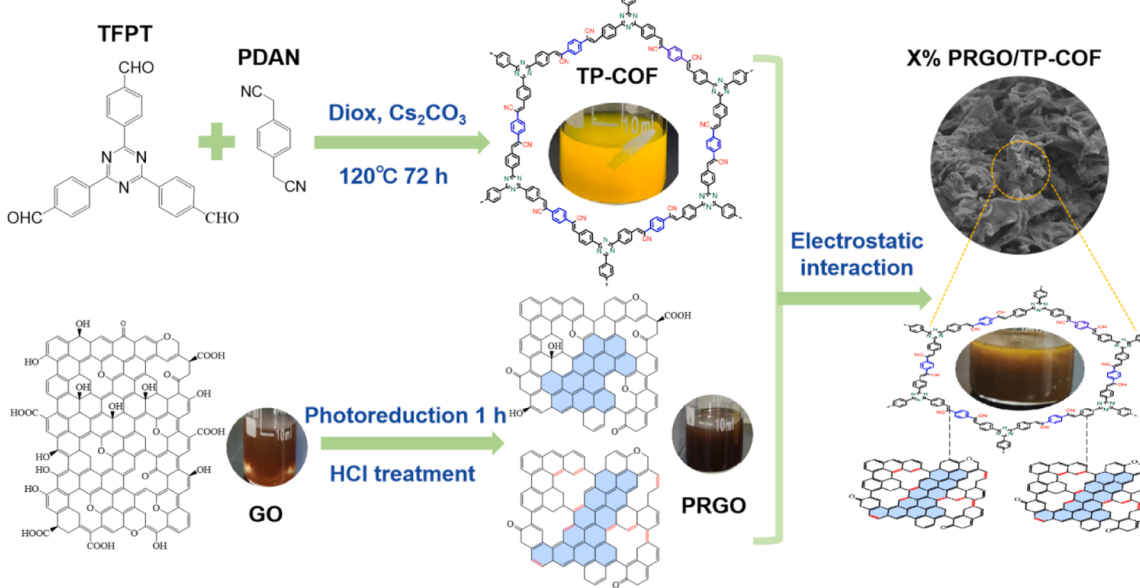


Fig. 1. The preparation process of PRGO/TP-COF nanocomposites.

UV-vis spectrophotometer (T6, Persee General, China) (5 mg of sample was deionised in 5 mL Milli-Q water, sonicated for 2 h, then diluted to 50 mg/L). Diffuse-reflectance UV-vis (DRUV-vis) spectra of TP-COF and 25% PRGO/TP-COF were recorded using a UV-3600PLUS Shimadzu spectrophotometer. Steady-state and transient-state Photoluminescence (PL) spectra were measured by a lifetime and steady state Fluorescence spectrometer (FLS980, Edinburgh Ltd., UK). The surface temperatures of samples were monitored by an infrared camera (H21PRO, Hikmicrotech., China).

2.4. Electron spin resonance (ESR) tests

The measurement of persistent free radicals (PFRs), photoelectron trapping and the detection of ·OH and ·O₂⁻ were performed on an electron spin resonance (ESR) spectrometer (EMXnano, Bruker, Germany). PFRs were measured as follows: 1 mg sample was dissolved in 1 mL Milli-Q water and sonicated for 1 h to obtain a suspension of 1 mg/mL, which was then transferred into a 1 mm glass capillary tube, blocked at both ends of the capillary tube with sealants, and placed directly into the inlet chamber of the ESR instrument for measurement. The modulation amplitude was 2.00 G and the attenuation was 19 dB. Regarding photoelectron trapping, 2,2,6,6-tetramethylpiperidin-1-yloxy (TEMPO) was used as the capture agent, and 100 µL sample suspension (2.5 mg mL⁻¹) was mixed well with 50 µL TEMPO (5 mmol L⁻¹) solution. The TEMPO signal intensity was measured at 0, 2, 5, and 10 min time points before and during visible light exposure. The modulation amplitude was 1.00 G, the attenuation was 25 dB, and the sweep time was 15 s. For ·OH and ·O₂⁻ detection, 5,5-dimethyl-1-pyrroline-N-oxide (DMPO) was used as the capture agent. 2 mg sample was dissolved in Milli-Q water or methanol, and the suspension was ultrasonically dispersed for 30 min. 40 µL sample suspension (2 mg mL⁻¹) was then mixed with 20 µL DMPO (20 mmol L⁻¹) solution. The test was carried out in the dark, and then irradiated under visible light for 15 min and measured again. The modulation amplitude was 2.00 G, the attenuation was 10 dB, and the sweep time was 40 s.

2.5. Photoelectrochemical tests

Mott-Schottky plots, cyclic voltammetry, photocurrent responses (PR), and electrochemical impedance spectroscopy (EIS) were tested on the electrochemical workstation (CHI700E, Shanghai Chenhua Instrument Co., Ltd. China) in a standard three-electrode cell with 0.1 mol/L Na₂SO₄ aqueous as the electrolyte. A saturated Ag/AgCl electrode was used as the reference electrode and Pt electrode as the counter electrode. 15 mg sample was sonicated for 30 min in 600 µL 5 wt% Nafion ethanol solution, and then 150 µL of the mixed solution was dropped onto indium tin oxide (ITO) conductive glass (1.5 cm × 1.2 cm) and dried at room temperature to obtain the working electrode.

2.6. Photocatalytic CO₂ reduction tests

The gas-solid photocatalytic CO₂ reduction reaction was carried out in a reaction system (Beijing Merry Change Co., Ltd., MC-SPB10) containing a 300 mL pyrex glass reactor, a 300 W Xe lamp with an ultra-violet cut filter ($\lambda > 400$ nm, with the light intensity output of 100 mW/cm²), a series of gas path and a pressure control system. The reaction took place at room temperature without additional heating. In each experiment, 5 mg sample was placed in the reactor and 1 mL Milli-Q water was injected. The system was evacuated for approximately 10 minutes until the water in the reactor was completely evaporated (water was no longer bubbling and pressure was maintained). After rinsing the entire system twice with high-purity CO₂ (99.99%), the CO₂ gas was introduced to bring the pressure to 0.13 MPa. Subsequently, the light source was switched on for photocatalytic CO₂ reduction. The gas-phase products were sampled every 30 min and analyzed using a gas chromatograph (GC9790II, Foley Analytical Instruments Ltd.) equipped

with a flame ionisation detector (FID) and a thermal conductivity detector (TCD). In addition, to ensure that the gas-phase products were produced by CO₂ reduction, high-purity nitrogen (N₂, 99.99%) was used instead of CO₂, and the experiments were carried out without changing the remaining steps. To investigate the stability of the materials, PRGO, TP-COF, and 25% PRGO/TP-COF were each subjected to four photocatalytic reduction cycles (20 h in total). After each photoreduction reaction, the reactor was cleaned, evacuated and then retested under the same experimental conditions as described above. The experimental product yields (µmol/g) was used as an index to evaluate the photocatalytic efficiency, and the yields data shown in the paper were the average of three replicate experiments.

3. Results and discussion

3.1. Characterization of samples

3.1.1. Morphology and structural features

There is electrostatic interaction between PRGO and TP-COF, so the agglomeration can be avoided when forming PRGO/TP-COF nanocomposites. The surface morphology and structure of TP-COF, PRGO, and 25% PRGO/TP-COF were characterized by FESEM. TP-COF showed a rod-like morphology (Fig. 2(a) and Fig. S1(a)), PRGO had large corrugated wrinkled nanosheets (Fig. 2(b) and Fig. S1(b)), whereas 25% PRGO/TP-COF resembled a “wood ear” (Fig. 2(c)). It may be due to the fact that the flaky PRGO wrapped the rod-shaped TP-COF (Fig. S1(c)), thus forming a twisted and folded “wood ear”. The TEM image further proved this conjecture with the rods and sheets closely stacked together (Fig. 2(d)), indicating that PRGO and TP-COF were successfully composited together through electrostatic interaction. As shown in Fig. 2(e-h), the mapping of FESEM further confirmed that the TP-COF was uniformly distributed on the PRGO nanosheets. 25% PRGO/TP-COF contained only three elements, C, N, and O (the elemental atomic ratios of 76.43%, 12.70%, and 10.87%, respectively) (Fig. S2), indicating that the synthesized nanocomposite owned high purity. Therefore, due to the similarity of the carbon skeleton of sp²-carbon conjugated TP-COF and PRGO, TP-COF was likely to be complexed with PRGO by surface charge modification and electrostatic self-assembly with π-π interactions, and good interfacial contacts were established.

The structure of the synthesized photocatalysts were determined by PXRD. As shown in Fig. S3(a), GO had a characteristic diffraction peak (001) at 11.9° [22], which was blue-shifted and the peak intensity decreased after photo-induced reduction, suggesting that photo-reduction led to a continuous reduction of oxygen-containing functional groups (OFGs) on the GO lamellae, and the nanosheets were efficiently exfoliated from each other, resulting in an increase in the interlayer spacing. In addition, a new diffraction peak around 29.1° (attributed to the graphene (G) characteristic diffraction peak (002) [23]) was also observed in PRGO, proving that GO after photoreduction had the characteristic peaks of both G and GO. The PXRD pattern of TP-COF showed four prominent peaks belonging to the planes of (100), (110), (200), and (210) at 2.9°, 4.8°, 6.3°, and 8.0°, respectively (Fig. S3 (a)). The (100) plane was of the highest atom density and exhibited the strongest peak signal, while the (110) plane had the second highest atomic density and thus the second strongest signal [24]. Their secondary planes (200) and (210) were also identified, indicating that the crystallinity of TP-COF synthesized in this study was pretty good. The full width at half peak (FWHM) of the main peak at 2θ = 2.9° is 0.62°, which was similar to the crystallinity of the previously reported TP-COF (0.74°) [25]. After the combination of TP-COF and PRGO, the PXRD pattern changed significantly, with three peaks located at 5.1°, 6.2°, 7.6° (showed in partial enlarged detail), 11.8°, and 28.3°, respectively (Fig. S3(a)). Therefore, 25% PRGO/TP-COF contained the characteristic peaks of both TP-COF and PRGO, indicating that the thermal-assisted electrostatic mutual attraction method used in this study was capable of combining TP-COF and PRGO.

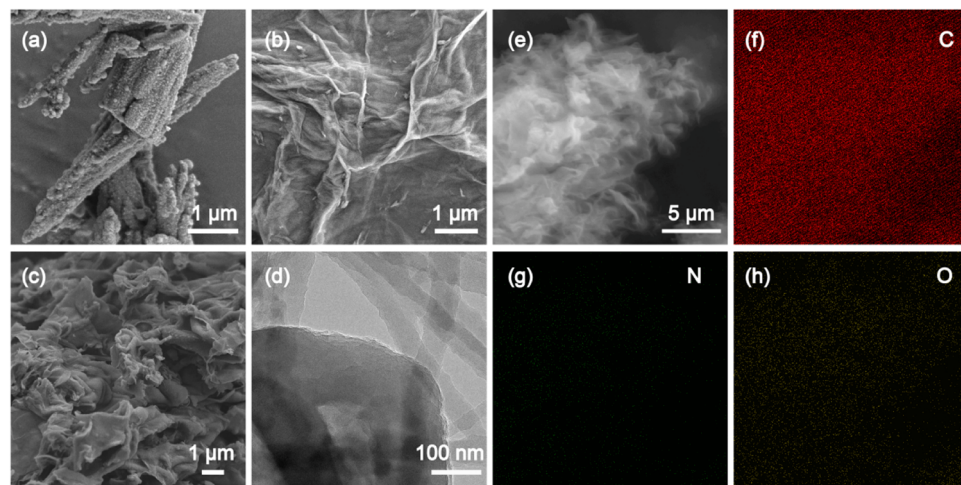


Fig. 2. FESEM images of TP-COF (a), PRGO (b), and 25% PRGO/TP-COF (c: 1 μm scale; e: 5 μm scale). TEM image of 25% PRGO/TP-COF (d). Distribution of C, N and O elements (f-h) based on 25% PRGO/TP-COF (e image).

The structure of the samples was further investigated using FT-IR. As shown in Fig. S3(b), the FT-IR spectrum of GO exhibited distinct absorption peaks of carboxyl ($\text{C}=\text{O}$), aromatic ring ($\text{C}=\text{C}$), hydroxyl ($\text{C}-\text{OH}$), epoxide ($\text{C}-\text{O}-\text{C}$), and alkoxy ($\text{C}-\text{O}$) at 1730, 1630, 1380, 1230, and 1040 cm^{-1} , respectively [26,27]. In the FT-IR spectrum of PRGO, all the characteristic peaks of OFGs on the GO lamellae layer were attenuated or disappeared, and the intensity of the $\text{C}=\text{C}$ peaks increased, suggesting that GO was reduced by light irradiation. Fig. 3(a) showed the FT-IR spectra of TP-COF and its two monomers, PDAN and TFPT. It can be seen that the cyano peak at 2214 cm^{-1} and the C-H peak at 2732 cm^{-1} were

found owing to PDAN and TFPT, respectively. Furthermore, a characteristic absorption peak of the triazine/benzene backbone at 1006 cm^{-1} was appeared, proving the successful polycondensation of PDAN and TFPT [24,25], achieving the construction of porous organic covalent backbone materials of TP-COF. When PRGO was compounded with TP-COF, the FT-IR spectrum of 25% PRGO/TP-COF (Fig. 3(a)) was almost the same as that of the TP-COF, and the characteristic peaks of the PRGO were overwhelmed by those of TP-COF. Notably, the sharp band at 807 cm^{-1} in the TP-COF caused by the breathing vibration of the tri-s-triazine units was red-shifted to a lower wavenumber of 805 cm^{-1}

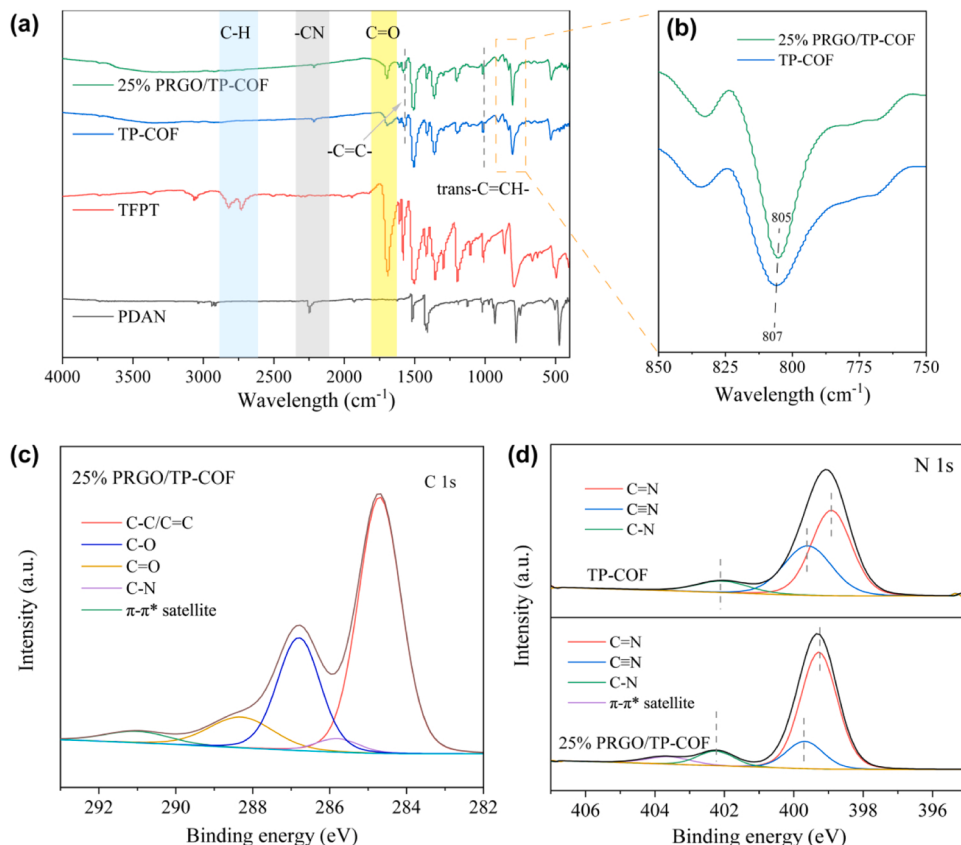


Fig. 3. FT-IR spectra of PDAN, TFPT, TP-COF and 25% PRGO/TP-COF (a). Enlarged FT-IR spectra corresponding to the orange rectangle (b). XPS C 1 s spectrum of 25% PRGO/TP-COF (c). N 1 s spectra of TP-COF and 25% PRGO/TP-COF (d).

in the 25% PRGO/TP-COF (Fig. 3(b)), suggesting that an interaction between PRGO and TP-COF was formed [28,29]. Combined with zeta potential, XRD and FT-IR analysis, GO can be reduced by light irradiation, and PRGO and TP-COF can be combined by electrostatic self-assembly of π - π interactions.

3.1.2. Surface functional group

XPS was used to further understand the elemental compositions and chemical states of TP-COF, PRGO, and 25% PRGO/TP-COF nanocomposites. For TP-COF, the C 1 s spectrum can be deconvoluted into three peaks with binding energies of 287.2, 286.2, and 284.6 eV, respectively (Fig. S4(a)). The peak at 287.2 eV was attributed to the N=C-N in the triazine ring [30], the peak at 286.2 eV corresponded to the C≡N in the cyano group, and the peak at 284.6 eV was attributed to C-C and C=C bonds. The C 1 s spectrum of PRGO can be deconvoluted into four peaks at 284.6, 286.8, 288.3 and 289.1 eV (Fig. S4(b)). They can be attributed to C-C and C=C bonds, a single-bonded oxygen group (C-OH/C-O-C), double-bonded carbon-oxygen group (C=O), and O-C=O in carboxylic acid or carboxylic anhydride [20], respectively. The presence of C-O and C=O peaks indicated that some OFGs still existed on the surface of PRGO after photo-induced reduction, which was consistent with the results of FT-IR. The C 1 s spectrum of 25% PRGO/TP-COF contained the features of TP-COG and PRGO (Fig. 3(c)), with five peaks corresponding to the C-C and C=C peaks at 284.6 eV, the C-N peak at 285.8 eV, the C-O peak at 286.8 eV, the C=O peak at 288.3 eV, and the π - π^* satellite peaks 291.0 eV [31–33]. Comparing the N 1 s spectra of TP-COF and 25% PRGO/TP-COF, TP-COF showed three peaks at 402.1, 399.6, and 398.9 eV (Fig. 3(d)) belonging to the nitrogen atoms in the C-N, C≡N, and C=N bonds, respectively [34], while 25% PRGO/TP-COF had a new π - π^* satellite peak at 403.7 eV [20], which further proved the existence of π - π interactions between PRGO and TP-COF. In addition, the characteristic peak position of N 1 s in 25% PRGO/TP-COF nanocomposites was about 0.1–0.3 eV higher than that in TP-COF, which was due to the decrease of the electron cloud density around N in TP-COF [35], suggesting the existed electrons transfer from TP-COF to PRGO. Based on the results of FESEM, TEM, XRD, FT-IR, and XPS analyses, it was demonstrated that compact heterojunctions were generated in 25% PRGO/TP-COF layered photocatalysts due to the strong coupling and π - π stacking interactions between TP-COF and PRGO.

3.1.3. Detection of defects and radicals

Raman spectra of GO and PRGO were performed to analyze the effect of photoreduction on GO defects. The planar vibrations of the sp^2 hybridized carbon atoms and the breathing modes of rings were manifested in the D and G bands of the Raman spectra, respectively. Meanwhile, the D and G bands also correspond to the defects and graphitization of graphene, respectively [36]. In addition, the intensity ratio of D and G bands (I_D/I_G) can reflect the graphene sheet defects content [37]. As shown in Fig. S5(a), the I_D/I_G of PRGO was 0.9457, which was larger than that of GO, indicating that the decrease of OFGs on the surface of GO resulted in the formation of small-scale sp^2 hybridization zones, causing a large number of defects [38–40]. Furthermore, persistent free radicals (PFRs) in GO, PRGO, TP-COF, and 25% PRGO/TP-COF were detected using ESR, and the results were shown in Fig. S5(b), where all the samples exhibited single peaks of carbon-centered radical with g-value around 2.0026 [41]. The content of PFRs in GO, PRGO, TP-COF, and 25% PRGO/TP-COF was 3.90×10^{12} , 4.62×10^{12} , 2.97×10^{10} , and 4.79×10^{12} spins/(mg mL⁻¹), respectively. Since the content of PFRs was associated with unpaired π -electron spins and high levels of intrinsic structural defects [42], the higher PFRs content of PRGO compared to GO implied a higher defects density, which was consistent with the Raman results. And the higher PFRs content exhibited in the 25% PRGO/TP-COF suggested that PRGO played a key role in enhancing the defects of the nanocomposites.

3.1.4. Light absorption properties and band structure

The appearances of GO and PRGO suspensions were shown in Fig. 1, where the brown solution was converted to a black solution after photoreduction, with a significant enhancement in light absorption. The UV-vis absorption spectra of both GO and PRGO showed a strong absorption peak near 230 nm and a small shoulder peak near 300 nm (Fig. 4(a)), which were attributed to the π - π^* transition of C=C and the n- π^* jump of OFGs, respectively [43], and the enhanced absorption intensity of PRGO compared to GO indicated the successful reduction of GO. Since GO was composed of sp^2 and sp^3 structural domains, the band gap was a range, which was obtained from Tauc plots, 3.37–4.31 eV for GO and slightly narrowed 3.14–4.22 eV for PRGO. The presence of the band gap supported the semiconducting properties of GO and PRGO, and both can be excited by visible light. The light absorption properties of TP-COF and 25% PRGO/TP-COF were investigated by DRUV-vis spectra, and 25% PRGO/TP-COF showed a greater light absorption range compared to TP-COF (Fig. 4(b and c)), and the increase in the light absorption capacity of the nanocomposites should be attributed to the introduction of PRGO. Based on the light absorption curves, the corresponding band gaps of TP-COF and 25% PRGO/TP-COF were obtained to be 2.38 and 1.75 eV, respectively. Therefore, PRGO as a conductive base immobilized TP-COF through a self-assembly strategy facilitated by surface charge, and this strategy enhanced the absorption of visible light by TP-COF and improved its photoexcitation efficiency. The valence band (VB vs. NHE) values of 1.43 eV and 2.59 eV for TP-COF and PRGO, respectively, were calculated from the XPS-VB test. In addition, the flat band potential (E_{fb}) of TP-COF was obtained from Mott-Schottky (MS) measurements at three different frequencies (Fig. 4(e)), with a positive slope indicating that TP-COF was an n-type semiconductor. Based on the MS measurements and considering that the conduction band (CB) value of n-type semiconductors were usually always 0.3 eV higher than E_{fb} [44,45], the CB value of TP-COF was calculated to be -0.97 eV, which was similar to that obtained by the difference (-0.95 eV) between the band gap value and the VB value. CB value of PRGO (-0.56 eV) was obtained using cyclic voltammetry, which was lower than the reduction potential of CO₂ (CO₂/CO at -0.53 V vs NHE), further demonstrating that PRGO can be used as a photocatalyst for CO₂ reduction.

3.1.5. Measurement of photogenerated reactive species

TEMPO was used as electrons capture agent to examine electron generation under visible light irradiation. No decrease in the TEMPO signal was observed in the blank experiments (visible light irradiation using TEMPO alone (Fig. S6(a)) or 25% PRGO/TP-COF + TEMPO in the dark (Fig. S6(b)). When 25% PRGO/TP-COF was added to TEMPO and exposed to visible light, the ESR signal gradually and significantly weakened with irradiation time (Fig. 5(a)), which was attributed to the binding of photogenerated electrons to TEMPO. The same experiments were carried out for the PRGO and TP-COF samples (Fig. S6(c and d)), and the slopes were obtained by linearly fitting the curves of TEMPO decay with time in order to compare the electron generation efficiencies. The photoelectron generation efficiencies of 25% PRGO/TP-COF were 2.01 and 1.82 times higher than those of PRGO and TP-COF, respectively (Fig. 5(b)), indicating that there may be carriers transfer between PRGO and TP-COF, which reduced the recombination of photogenerated carriers and made more electrons available.

The Steady-state PL spectrum of TP-COF showed an intense emission peak at around 560 nm, and the intensity of this emission peak was decreased when PRGO was introduced (Fig. 5(c)), which indicated the recombination of electron(e⁻)-hole(h⁺) pairs was significantly lessened. This may be attributed to the carries transfer at the heterojunction between TP-COF and PRGO [29,46,47]. The transient-state PL spectra showed that the average PL lifetime of TP-COF was 15.92 ns, which decreased to 10.80 ns in 25% PRGO/TP-COF (Fig. 5(d)). The multi-exponential fit of TP-COF presented a double-exponential curve corresponding to free charge lifetime ($\tau_1 = 4.68$ ns, 75.05%) and trapping lifetime ($\tau_2 = 22.89$ ns, 24.95%) [48]. Due to the transfer of some

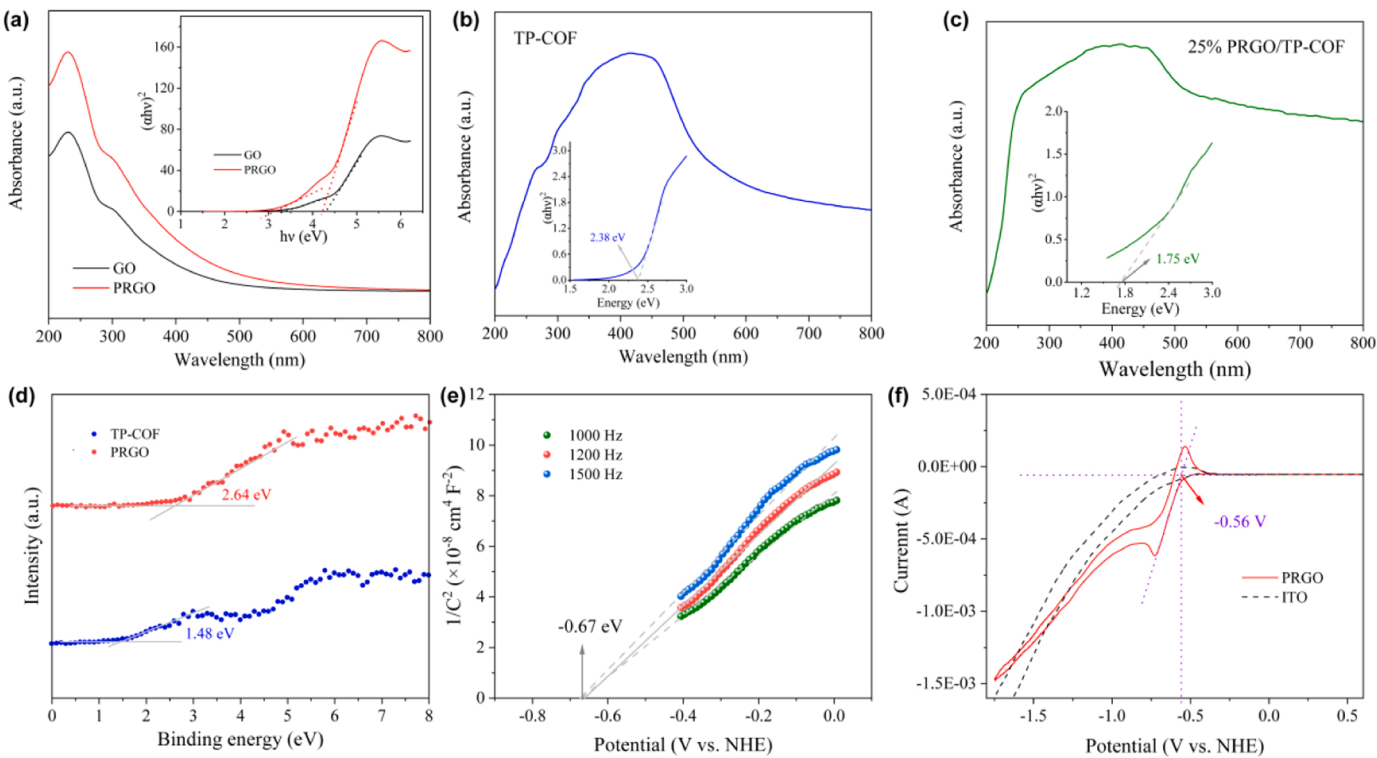


Fig. 4. UV-vis spectra of GO and PRGO samples (corresponding Tauc plots shown in inset) (a). DRUV-vis spectra of TP-COF (b) and 25% PRGO/TP-COF (c) (corresponding Tauc plot in inset). XPS valence band potentials of PRGO and TP-COF (d). Mott–Schottky curve of TP-COF (e). Cyclic voltammetry of PRGO and reduction onset potential (f).

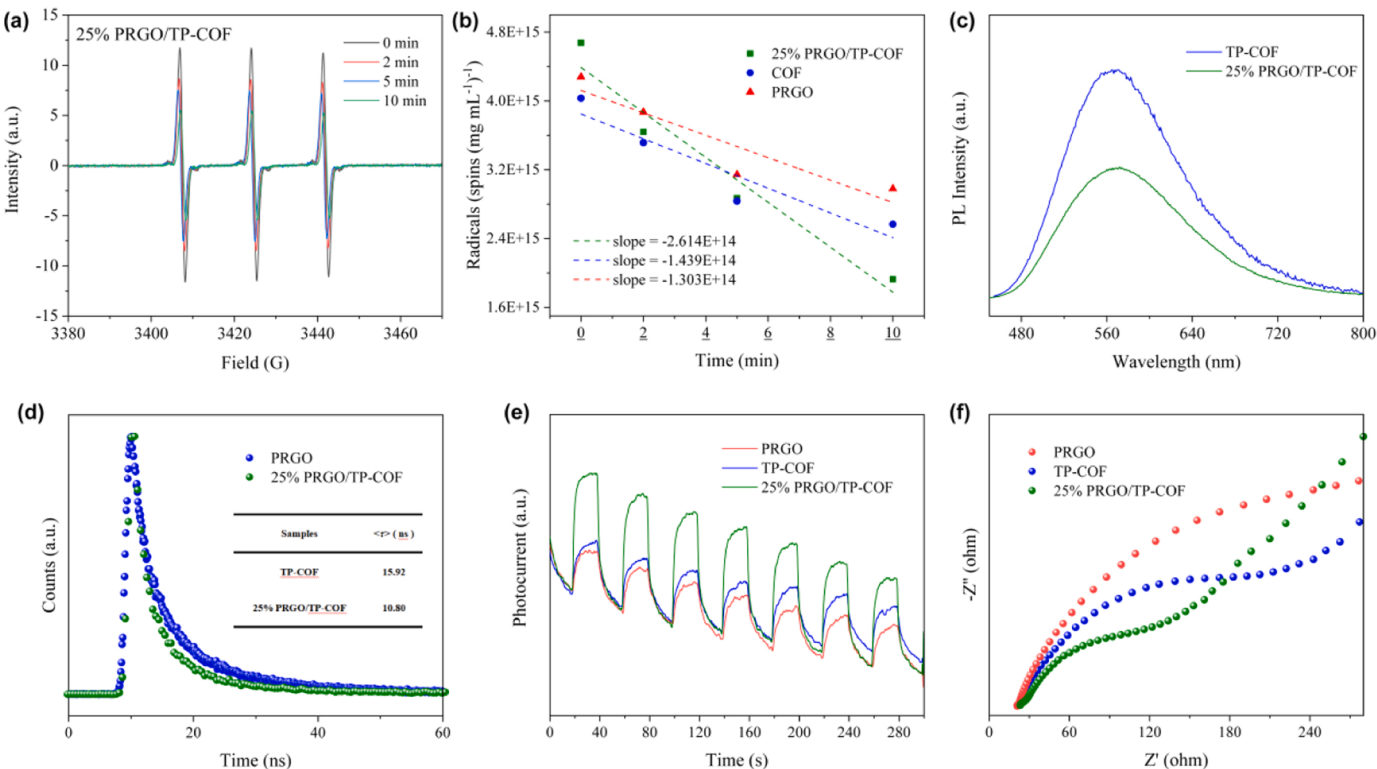


Fig. 5. ESR signals of 25% PRGO/TP-COF+TEMPO at 0, 2, 5, and 10 min under visible light irradiation (a). Linear fitting of ESR signals to visible light exposure time (b). Steady-state (c) and transient-state (d) PL spectra of TP-COF and 25% PRGO/TP-COF. Photocurrent response (e) and Nyquist plots (f) of PRGO, TP-COF, and 25% PRGO/TP-COF.

electrons from TP-COF to PRGO (as analyzed in XPS), the free charge lifetime ($\tau_1 = 4.32$ ns, 52.74%) and trapping lifetime ($\tau_2 = 13.07$ ns, 47.26%) decreased in 25% PRGO/TP-COF, suggesting a change in the energy band structure of the COF when it was complexed with PRGO. The proportion of free charge lifetime in 25% PRGO/TP-COF decreased when compared with that of the TP-COF, indicating that the recombination of photogenerated charges in 25% PRGO/TP-COF was suppressed [49], which was conducive to the improvement of photocatalytic

activity. The effect of the heterojunction structure of 25% PRGO/TP-COF photocatalyst on the photogenerated e⁻-h⁺ pairs separation efficiency was investigated by photocurrent response (PR) and electrochemical impedance spectroscopy (EIS). The PR average value of 25% PRGO/TP-COF was 2.69 and 1.96 times higher than those of PRGO and TP-COF, respectively (Fig. 5(e)), suggesting that the composites have the highest amount of photogenerated electrons, which was in agreement with the results obtained by TEMPO. In addition, Fig. 5(f)

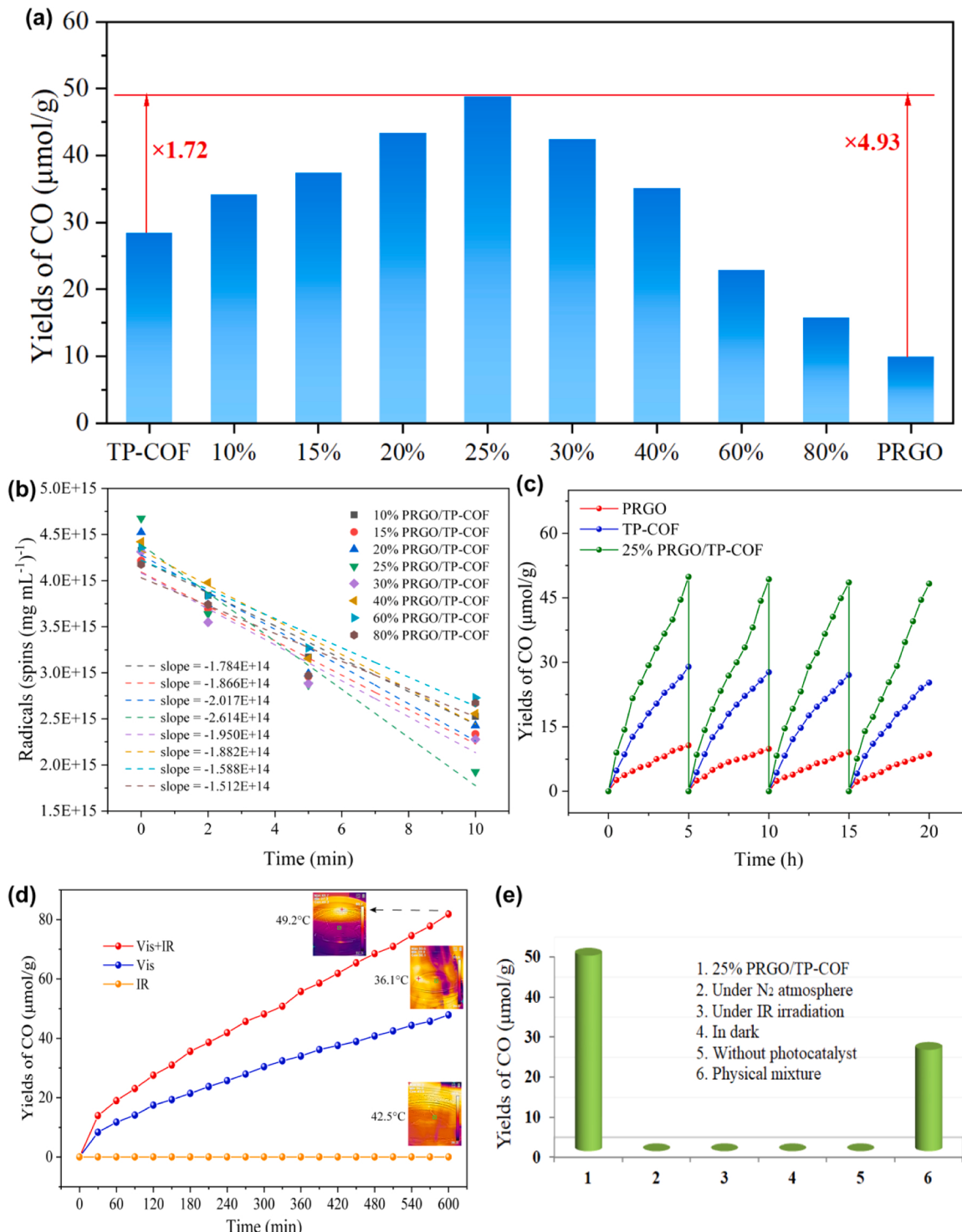


Fig. 6. CO yields of TP-COF, PRGO and X% PRGO/TP-COF (a). Linear fitting of ESR signals to visible light irradiation time of TEMPO in X% PRGO/TP-COF samples (b). Comparison of photocatalytic cycle performance of TP-COF, PRGO and 25% PRGO/TP-COF (c). CO yields of 25% PRGO/TP-COF in photocatalytic CO₂ reduction under different light sources (d). CO yields of 25% PRGO/TP-COF under different experimental conditions (e).

showed that 25% PRGO/TP-COF had the smallest radius, which indicated that the sample had the smallest electrical resistance and was able to separate and transfer the photogenerated charges quickly. The above results confirmed that the 25% PRGO/TP-COF composite was capable of efficient carriers separation and transfer.

3.2. CO_2 photocatalytic reduction activity

The photocatalytic reductions of CO_2 by TP-COF, PRGO, and X% PRGO/TP-COF were carried out under co-irradiation of visible and infrared light using saturated water vapour as the reductant without sacrificial agent and photosensitizer. As shown in Fig. 6(a), the CO yields were 34.20, 37.40, 43.45, 48.81, 42.46, 35.18, 22.96, and 15.81 $\mu\text{mol/g}$ at 10%, 15%, 20%, 25%, 30%, 40%, 60%, and 80% of the PRGO mass share, respectively. It was observed that on the photocatalytic CO_2 reduction abilities of X% PRGO/TP-COF composites were consistent with those photogenerated electrons generation efficiencies (measured by the decay rates of TEMPO (Fig. 6(b)), which indicated that the amount of photogenerated electrons could directly affect the CO_2 reduction activity. Compared with pure TP-COF and PRGO, nanocomposites with appropriate ratios (PRGO mass share <50%) can improve the CO_2 reduction efficiency. 25% PRGO/TP-COF had the best photocatalytic reduction effect, which was 1.72 times more than that of pure TP-COF, and 4.93 times more than that of pure PRGO. Therefore, appropriate doping ratios of TP-COF and PRGO were required to achieve effective and tight interfacial contact, accelerated carriers separation, and increased the photogenerated electrons content, thus presenting optimal photocatalytic activity in the process of CO generation. The photocatalytic CO_2 reduction performance of this binary metal-free composite was better than some semiconductor/COF composite systems and even ternary composite systems (Table S1), while the metal-free properties and simple synthetic method made the photocatalysts designed in this study more environmentally friendly and economical. Fig. 6(c) compared the photocatalytic reduction stability of TP-COF, PRGO, and 25% PRGO/TP-COF catalysts. In four repetitive cycling experiments, the CO yields of the fourth time of TP-COF, PRGO, and 25% PRGO/TP-COF were reduced by 18.47%, 12.75%, and 3.21% compared to the first time, indicating that the composites had better stability compared with single material. In addition, by subjecting the 25% PRGO/TP-COF after 10 h of reaction to FT-IR characterization, it was almost similar to the pre-reaction profile, with only a slight decrease in peak intensity (Fig. S7), indicating that the 25% PRGO/TP-COF had a certain stability. Furthermore, photocatalytic CO_2 reduction tests of 25% PRGO/TP-COF were conducted for 10 h under the irradiation of three light sources: visible only (Vis), visible + infrared (Vis+IR), and infrared only (IR) (Fig. 6(d)). No CO was detected under IR irradiation, indicating that the generation of CO was dependent on visible light. The CO yields obtained by Vis+IR irradiation was significantly higher than that obtained by Vis irradiation, suggesting that IR was beneficial to improve the efficiency of photocatalytic CO_2 reduction, which should be attributed to the photo-thermal effect of PRGO [50–52]. The average surface temperatures of the samples were 36.1, 42.5, and 49.2°C after 10 h irradiation with Vis, IR, and Vis+IR light sources (with the same irradiation intensity), respectively, which indicated that PRGO could absorb IR and released heat to increase the surface temperature. The higher temperature can reduce the reaction energy barrier of CO_2 and accelerate the separation and migration of carriers, so it made the CO_2 reduction reaction faster and more efficient [53,54]. Through the photocatalytic test of 25% PRGO/TP-COF in N_2 atmosphere (other experimental conditions remained unchanged, only CO_2 gas was replaced with N_2), no CO generation was detected during the 5 h reaction time (Fig. 6(e)), indicating that the CO obtained in this study originated from the conversion of CO_2 . In addition, by physically mixing PRGO with TP-COF at a mass ratio of 1:3 by grinding and then testing the photocatalytic reduction of CO_2 under the same conditions, CO yields (25.31 $\mu\text{mol/g}$) was significantly lower than that of 25% PRGO/TP-COF (Fig. 6(e)),

which further demonstrated that the synthesis method used in this study was capable of combining the PRGO and TP-COF via π - π interaction and formed heterojunction.

3.3. Mechanism analysis for CO_2 photoreduction

To investigate the carriers transfer mechanism in the 25% PRGO/TP-COF heterojunction, the work function (Φ) of PRGO and TP-COF was determined by the UPS technology, and the values of Φ were obtained to be 5.23 and 4.90 eV for PRGO and TP-COF, respectively (Fig. S8) [55], which indicated that the Fermi energy level (E_f) of PRGO was lower than the E_f position of TP-COF. Therefore, when they were in close contact, the free electrons in TP-COF spontaneously slid across the interface to reach PRGO after intimate contact. This process reached equilibrium when the electron densities of the two were aligned, which resulted in the aggregation of electrons at the interface of PRGO and a concomitant decrease in the electron density at the interface of TP-COF, which was in agreement with the XPS results. As a result, the energy band of PRGO bent downward while the energy band of TP-COF bent upward. At the same time, an internal electric field (IEF) pointing from TP-COF to PRGO was formed at the interface. This IEF can provide a strong driving force for the transfer of photogenerated electrons from PRGO to TP-COF. Therefore, the photogenerated electrons on the CB of PRGO and the photogenerated holes on the VB of TP-COF recombined, leaving the strongly reducing electrons on the CB of TP-COF and the strongly oxidizing holes on the VB of PRGO. Therefore, this S-scheme transfer mechanism collectively achieved charges separation and maximized redox capacity [56–58], providing a strong driving force for 25% PRGO/TP-COF photocatalytic reduction of CO_2 .

The S-scheme heterojunction of 25% PRGO/TP-COF was further confirmed by electron spin resonance (ESR) probing of spin-active $\cdot\text{OH}$ ($\text{H}_2\text{O}/\cdot\text{OH} = -2.27$ V vs NHE) and $\cdot\text{O}_2^-$ ($\text{O}_2^-/\cdot\text{O}_2^- = -0.33$ V vs NHE) using DMPO as trapping agent [59,60]. The ESR spectra of DMPO- $\cdot\text{O}_2^-$ signal under visible irradiation were shown in Fig. 7(a), and the characteristic signal of DMPO- $\cdot\text{O}_2^-$ was observed for all the tested samples, indicating that the photogenerated electrons in all the samples have the ability to reduce O_2 to form $\cdot\text{O}_2^-$. The ESR spectra of DMPO- $\cdot\text{OH}$ signal were shown in Fig. 7(b), and it can be seen that the PRGO and 25% PRGO/TP-COF exhibited characteristic signals of DMPO- $\cdot\text{OH}$, while TP-COF did not exhibit a significant signal. The absence of DMPO- $\cdot\text{OH}$ signal in TP-COF can be attributed to the low oxidation potential of photoexcited holes in TP-COF, which made it difficult to convert H_2O or hydroxyl ions to $\cdot\text{OH}$. Notably, the signals of DMPO- $\cdot\text{O}_2^-$ and DMPO- $\cdot\text{OH}$ signals in 25% PRGO/TP-COF were significantly stronger than those of single catalysts, indicating that more strongly reducing electrons and strongly oxidizing holes were retained due to the presence of S-scheme heterojunction.

Based on the above discussion, the mechanism of 25% PRGO/TP-COF photocatalysts for photocatalytic CO_2 reduction can be described in Fig. 8. Under light irradiation, the electrons in the VB of PRGO and TP-COF were photoexcited to the CB, while leaving holes in the VB (Eqs. 1–2). Due to the formation of S-scheme heterojunction, the internal electric field can be successfully constructed to bend the energy bands. Therefore, the photogenerated electrons in the CB of PRGO were transferred to the interface and quenched by the photogenerated holes in the VB of TP-COF. As a result, the strongly oxidizing holes were retained in PRGO, which was able to oxidize H_2O to form H^+ (Eq. 3); meanwhile, the strongly reducing photogenerated electrons were retained in the CB of TP-COF, which was involved in the reduction of CO_2 to CO with the participation of H^+ (Eq. 4). In addition, due to the release of heat by the absorption of IR by PRGO, the thermoelectrons generated by PRGO were able to rapidly recombine with the holes of TP-COF, so that more electrons in TP-COF can be retained and utilized. Moreover, the heat on the catalyst surface can accelerate the adsorption and activation of CO_2 , as well as the desorption of the product [61,62], and lower the energy barrier of the reduction reaction, so that the reduction of CO_2 to CO can be carried out more efficiently. Thus, thanks

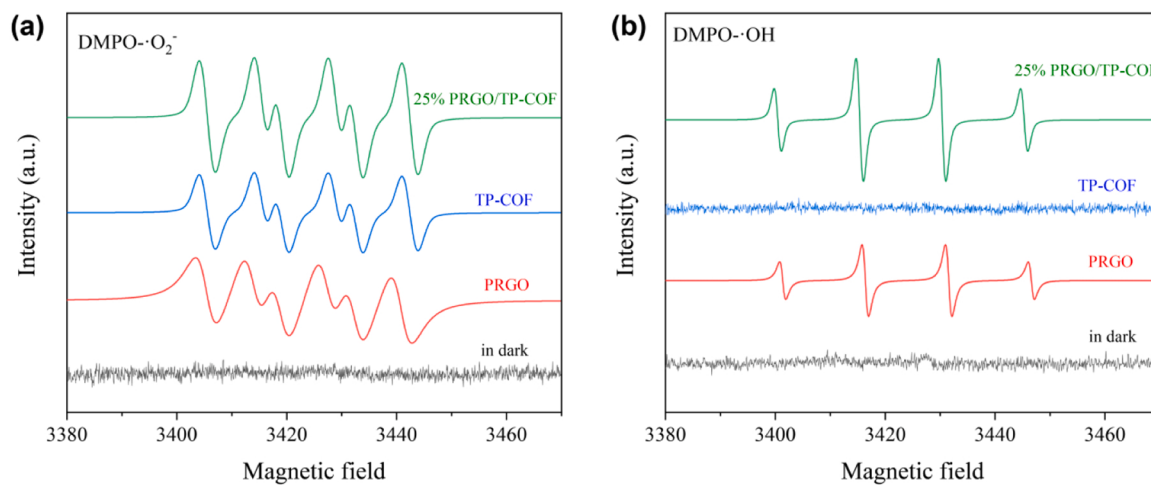


Fig. 7. ESR spectra of DMPO-·O₂ (a) in methanol solution and DMPO-OH (b) in aqueous solution in the presence of PRGO, TP-COF, and 25% PRGO/TP-COF.

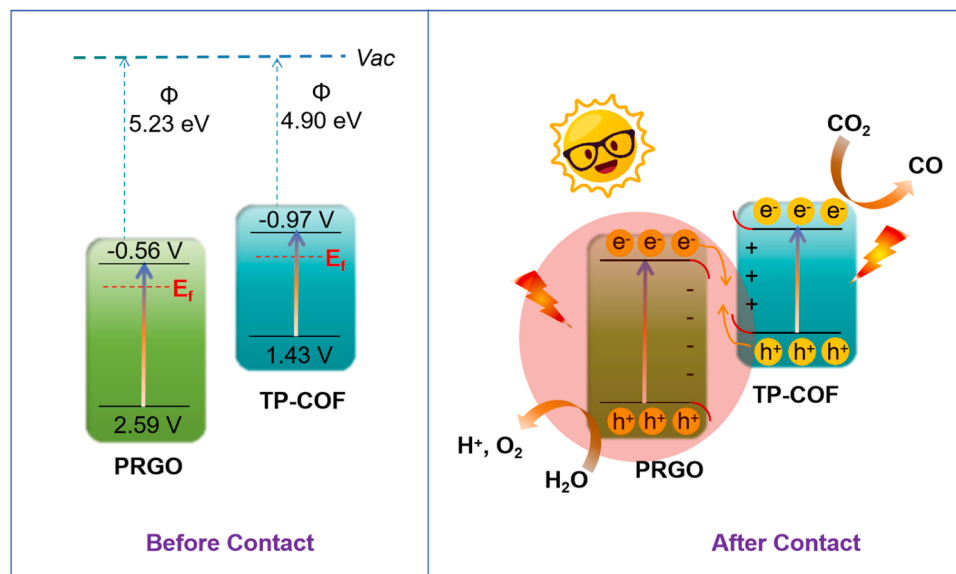
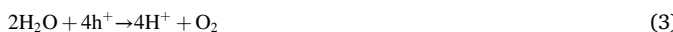
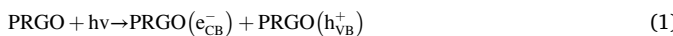


Fig. 8. Mechanism of photocatalytic CO₂ reduction by 25% PRGO/TP-COF nanocomposites under light irradiation.

to the synergistic effect of the S-scheme transfer mechanism and photothermal effect, 25% PRGO/TP-COF metal-free composite photocatalyst exhibited excellent photocatalytic ability.



4. Conclusions

In this work, a novel organic-inorganic composite metal-free heterojunction photocatalyst was constructed by a simple and green electrostatic self-assembly method of combining PRGO with TP-COF. The PRGO and TP-COF were able to be excited under visible light to generate photogenerated carriers, and carried out migration according to the S-scheme mechanism, which achieved the effective spatial separation of charges and enabled enough electrons to reduce CO₂. In addition, with the assistance of IR heat, the hot electrons generated by PRGO promote

carriers separation due to the photothermal effect, which reduced the recombination of photogenerated e⁻-h⁺ pairs. Therefore, based on the synergistic effect of the photothermal effect of PRGO and the heterojunction between PRGO and TP-COF, 25% PRGO/TP-COF had excellent CO yields (48.81 μmol/g). This work provides a new idea for the design of economic and environmental friendly GO-based metal-free composite material for environment and energy applications.

CRediT authorship contribution statement

Yuhan Liu: Investigation, Data curation, Methodology, Formal analysis, Writing—original draft. **Yue Wang:** Investigation, Methodology. **Jing Shang:** Conceptualization, Formal analysis, Funding acquisition, Supervision, Writing – review & editing. **Jing Peng:** Funding acquisition, Writing – review & editing. **Tong Zhu:** Writing – review & editing.

Declaration of Competing Interest

The authors declare that they have no known competing financial interests or personal relationships that could have appeared to influence

the work reported in this paper.

Data Availability

Data will be made available on request.

Acknowledgments

The authors are grateful to the financial support provided by the New Engineering Cross-project of Peking University (No. 7100604008), the National Key Research and Development Program of China (No. 2022YFC3701104).

Appendix A. Supporting information

Supplementary data associated with this article can be found in the online version at [doi:10.1016/j.apcatb.2024.123937](https://doi.org/10.1016/j.apcatb.2024.123937).

References

- [1] Y. Yang, H.-Y. Zhang, Y. Wang, L.-H. Shao, L. Fang, H. Dong, M. Lu, L.-Z. Dong, Y.-Q. Lan, F.-M. Zhang, Integrating Enrichment, Reduction, and Oxidation Sites in One System for Artificial Photosynthetic Diluted CO₂ Reduction, *Adv. Mater.* 35 (2023) 2304170.
- [2] C. Gao, J. Low, R. Long, T. Kong, J. Zhu, Y. Xiong, Heterogeneous single-atom photocatalysts: fundamentals and applications, *Chem. Rev.* 120 (2020) 12175–12216.
- [3] S. Yoshino, T. Takayama, Y. Yamaguchi, A. Iwase, A. Kudo, CO₂ Reduction using water as an electron donor over heterogeneous photocatalysts aiming at artificial photosynthesis, *Acc. Chem. Res.* 55 (2022) 966–977.
- [4] E. Jin, Z. Lan, Q. Jiang, K. Geng, G. Li, X. Wang, D. Jiang, 2D sp² Carbon-conjugated covalent organic frameworks for photocatalytic hydrogen production from water, *Chem* 5 (2019) 1632–1647.
- [5] X.D. Sun, H.W. Huang, Q. Zhao, T.Y. Ma, L.Z. Wang, Thin-layered photocatalysts, *Adv. Funct. Mater.* 30 (2020) 1910005.
- [6] Z.S. Chen, J.Y. Wang, M.J. Hao, Y.H. Xie, X.L. Liu, H. Yang, G.I.N. Waterhouse, X. K. Wang, S.Q. Ma, Tuning excited state electronic structure and charge transport in covalent organic frameworks for enhanced photocatalytic performance, *Nat. Commun.* 14 (2023) 1106.
- [7] L. Dai, A.W. Dong, X.J. Meng, H.Y. Liu, Y.T. Li, P.F. Li, B. Wang, Enhancement of visible-light-driven hydrogen evolution activity of 2D π-conjugated bipyridine-based covalent organic frameworks via post-protonation, *Angew. Chem. -Int. Ed.* 62 (2023) e2023002.
- [8] W. Chen, L. Wang, D. Mo, F. He, Z. Wen, X. Wu, H. Xu, L. Chen, Modulating benzothiadiazole-based covalent organic frameworks via halogenation for enhanced photocatalytic water splitting, *Angew. Chem. -Int. Ed.* 59 (2020) 16902–16909.
- [9] R.F. Chen, Y. Wang, Y. Ma, A. Mal, X.Y. Gao, L. Gao, L.J. Qiao, X.B. Li, L.Z. Wu, C. Wang, Rational design of isostructural 2D porphyrin-based covalent organic frameworks for tunable photocatalytic hydrogen evolution, *Nat. Commun.* 12 (2021) 1354.
- [10] H. Shanavaz, N. Kannanugu, D. Kasai, K.Y. Kumar, M.S. Raghu, M.K. Prashanth, M. A. Khan, B.H. Jeon, E. Linul, Covalent organic frameworks as promising materials: review on synthetic strategies, topology and application towards supercapacitors, *J. Energy Storage* 71 (2023) 108006.
- [11] R. Chen, J.-L. Shi, Y. Ma, G. Lin, X. Lang, C. Wang, Designed synthesis of a 2D porphyrin-based sp² carbon-conjugated covalent organic framework for heterogeneous photocatalysis, *Angew. Chem. -Int. Ed.* 58 (2019) 6430–6434.
- [12] J. Xu, C. Yang, S. Bi, W. Wang, Y. He, D. Wu, Q. Liang, X. Wang, F. Zhang, Vinylene-linked covalent organic frameworks (Cofs) with symmetry-tuned polarity and photocatalytic activity, *Angew. Chem. -Int. Ed.* 59 (2020) 23845–23853.
- [13] Z. Zhang, J. Jia, Y. Zhi, S. Ma, X. Liu, Porous organic polymers for light-driven organic transformations, *Chem. Soc. Rev.* 51 (2022) 2444–2490.
- [14] Z.P. Li, J.A. Wang, S. Ma, Z.W. Zhang, Y.F. Zhi, F.C. Zhang, H. Xia, G. Henkelman, X.M. Liu, 2D covalent organic frameworks for photosynthesis of A-trifluoromethyl ketones from aromatic alkenes, *Appl. Catal. B-Environ.* 310 (2022) 121335.
- [15] M. Zhang, M. Lu, Z.-L. Lang, J. Liu, M. Liu, J.-N. Chang, L.-Y. Li, L.-J. Shang, M. Wang, S.-L. Li, Y.-Q. Lan, Semiconductor/covalent-organic-framework Z-scheme heterojunctions for artificial photosynthesis, *Angew. Chem. -Int. Ed.* 59 (2020) 6500–6506.
- [16] H. Zhong, R.J. Sa, H.W. Lv, S.L. Yang, D.Q. Yuan, X.C. Wang, R.H. Wang, Covalent organic framework hosting metalloporphyrin-based carbon dots for visible-light-driven selective CO₂ reduction, *Adv. Funct. Mater.* 30 (2020) 2002654.
- [17] Y. Liu, J. Shang, T. Zhu, Enhanced thermal-assisted photocatalytic CO₂ reduction by RGO/H-CN two-dimensional heterojunction, *J. Mater. Sci. Technol.* 176 (2024) 36–47.
- [18] Y. Kuang, J. Shang, T. Zhu, Photoactivated graphene oxide to enhance photocatalytic reduction of CO₂, *ACS Appl. Mater. Inter* 12 (2020) 3580–3591.
- [19] V.N. Gopalakrishnan, D.T. Nguyen, J. Becerra, M. Sakar, T.O. Do, Manifestation of an enhanced photoreduction of CO₂ to CO over the in situ synthesized rGO-covalent organic framework under visible light irradiation, *ACS Appl. Energ. Mater.* 4 (2021) 6005–6014.
- [20] Y.-H. Yao, Y. Yang, Y. Wang, H. Zhang, H.-L. Tang, H.-Y. Zhang, G. Zhang, Y. Wang, F.-M. Zhang, H. Yan, Photo-induced synthesis of ternary Pt/rGO/COF photocatalyst with Pt nanoparticles precisely anchored on rGO for efficient visible-light-driven H₂ evolution, *J. Colloid Interf. Sci.* 608 (2022) 2613–2622.
- [21] Y.-H. Yao, J. Li, H. Zhang, H.-L. Tang, L. Fang, G.-D. Niu, X.-J. Sun, F.-M. Zhang, Facile synthesis of a covalently connected rGO-COF hybrid material by in situ reaction for enhanced visible-light induced photocatalytic H₂ evolution, *J. Mater. Chem. A* 8 (2020) 8949–8956.
- [22] T.-F. Yeh, F.-F. Chan, C.-T. Hsieh, H. Teng, Graphite oxide with different oxygenated levels for hydrogen and oxygen production from water under illumination: the band positions of graphite oxide, *J. Phys. Chem. C* 115 (2011) 22587–22597.
- [23] J. Shen, Y. Hu, M. Shi, X. Lu, C. Qin, C. Li, M. Ye, Fast and facile preparation of graphene oxide and reduced graphene oxide nanoplatelets, *Chem. Mater.* 21 (2009) 3514–3520.
- [24] Y. Zhao, H. Liu, C. Wu, Z. Zhang, Q. Pan, F. Hu, R. Wang, P. Li, X. Huang, Z. Li, Fully Conjugated two-dimensional sp²-carbon covalent organic frameworks as artificial photosystem i with high efficiency, *Angew. Chem. -Int. Ed.* 58 (2019) 5376–5381.
- [25] S. Ma, T.Q. Deng, Z.P. Li, Z.W. Zhang, J. Jia, G. Wu, H. Xia, S.W. Yang, X.M. Liu, Photocatalytic hydrogen production on a sp²-carbon-linked covalent organic framework, *Angew. Chem. -Int. Ed.* 61 (2022) e202208919.
- [26] R.F. Albers, R.A. Bini, J.B. Souza Jr., D.T. Machado, L.C. Varanda, A general one-pot synthetic strategy to reduced graphene oxide (rGO) and rGO-nanoparticle hybrid materials, *Carbon* 143 (2019) 73–84.
- [27] J. Zhang, H. Yang, G. Shen, P. Cheng, J. Zhang, S. Guo, Reduction of graphene oxide via L-ascorbic acid, *Chem. Commun.* 46 (2010) 1112–1114.
- [28] Y. Zhang, T. Mori, L. Niu, J. Ye, Non-covalent doping of graphitic carbon nitride polymer with graphene: controlled electronic structure and enhanced optoelectronic conversion, *Energy Environ. Sci.* 4 (2011) 4517–4521.
- [29] W.-J. Ong, L.-L. Tan, S.-P. Chai, S.-T. Yong, A.R. Mohamed, Surface charge modification via protonation of graphitic carbon nitride (g-C₃N₄) for electrostatic self-assembly construction of 2D/2D reduced graphene oxide (rGO)/g-C₃N₄ nanostructures toward enhanced photocatalytic reduction of carbon dioxide to methane, *Nano Energy* 13 (2015) 757–770.
- [30] X.L. Hu, Z. Zhan, J.Q. Zhang, I. Hussain, B.E. Tan, Immobilized covalent triazine frameworks films as effective photocatalysts for hydrogen evolution reaction, *Nat. Commun.* 12 (2021) 6596.
- [31] S.Y. Ou, M. Zhou, W. Chen, Y.Y. Zhang, Y.L. Liu, COF-5/CoAl-LDH nanocomposite heterojunction for enhanced visible-light-driven CO₂ reduction, *Chemsuschem* 15 (2022) e202200184.
- [32] J. Wang, L. Wang, D. Zhang, Y. Wang, J. Li, F. Zhou, J. Huang, Y.-N. Liu, Covalently connected core-shell NH₂-MIL-125@COFs-OH Hybrid Materials for Visible-Light-Driven CO₂ reduction, *J. Colloid Interf. Sci.* 637 (2023) 1–9.
- [33] Y.H. Wu, J.S. Liu, J. Rong, Y.Z. Zhang, Q. Liang, M. Zhou, Z.Y. Li, S. Xu, Combination of covalent-organic framework and Bi₂O₃S by covalent bonds to form P-N heterojunction for enhanced photocatalytic CO₂ conversion, *Appl. Surf. Sci.* 620 (2023) 156781.
- [34] X. Zhuang, W. Zhao, F. Zhang, Y. Cao, F. Liu, S. Bia, X. Feng, A two-dimensional conjugated polymer framework with fully sp²-bonded carbon skeleton, *Polym. Chem.* 7 (2016) 4176–4181.
- [35] H.J. Zhu, Z.H. Chen, Y.Y. Hu, L.X. Gong, D.D. Li, Z.K. Li, A. Novel, Immobilized Z-Scheme P₃IHT-α-Fe₂O₃ photocatalyst array: study on the excellent photocatalytic performance and photocatalytic mechanism, *J. Hazard. Mater.* 389 (2020) 122119.
- [36] J.-B. Wu, M.-L. Lin, X. Cong, H.-N. Liu, P.-H. Tan, Raman spectroscopy of grapheme-based materials and its applications in related devices, *Chem. Soc. Rev.* 47 (2018) 1822–1873.
- [37] L.M. Malard, M.A. Pimenta, G. Dresselhaus, M.S. Dresselhaus, Raman spectroscopy in graphene, *Phys. Rep.-Rev. Sec. Phys. Lett.* 473 (2009) 51–87.
- [38] S. Park, R.S. Ruoff, Chemical methods for the production of graphenes, *Nat. Nanotechnol.* 4 (2009) 217–224.
- [39] Y.Q. Zeng, T. Li, Y.G. Yao, T.Y. Li, L.B. Hu, A. Marconnet, Thermally conductive reduced graphene oxide thin films for extreme temperature sensors, *Adv. Funct. Mater.* 29 (2019) 1901388.
- [40] R. Liu, Y. Zhang, Z. Ning, Y. Xu, A Catalytic microwave process for superfast preparation of high-quality reduced graphene oxide, *Angew. Chem. -Int. Ed.* 56 (2017) 15677–15682.
- [41] B. Dellinger, S. Lominicki, L. Khachaturyan, Z. Maskos, R.W. Hall, J. Adounkpe, C. McFerrin, H. Truong, Formation and stabilization of persistent free radicals, *Proc. Combust. Inst.* 31 (2007) 521–528.
- [42] O. Ivancic, D.J. Klein, L. Bytautas, Unpaired Pi-Spin Density in Defected Graphite, *Carbon* 40 (2002) 2063–2083.
- [43] D.G. Goodwin Jr., A.S. Adeleye, L. Sung, K.T. Ho, R.M. Burgess, E.J. Petersen, Detection and Quantification of Graphene-Family Nanomaterials in the Environment, *Environ. Sci. Technol.* 52 (2018) 4491–4513.
- [44] F.-M. Zhang, J.-L. Sheng, Z.-D. Yang, X.-J. Sun, H.-L. Tang, M. Lu, H. Dong, F.-C. Shen, J. Liu, Y.-Q. Lan, Rational Design of MOF/COF Hybrid Materials for Photocatalytic H₂ Evolution in the Presence of Sacrificial Electron Donors, *Angew. Chem. -Int. Ed.* 57 (2018) 12106–12110.
- [45] F. Xu, C. Lai, M. Zhang, B. Li, S. Liu, M. Chen, L. Li, Y. Xu, L. Qin, Y. Fu, X. Liu, H. Yi, X. Yang, Facile One-Pot Synthesis of Carbon Self-Doped Graphitic Carbon Nitride Loaded with Ultra-Low Ceric Dioxide for High-Efficiency Environmental

- Photocatalysis: Organic Pollutants Degradation and Hexavalent Chromium Reduction, *J. Colloid Interface Sci.* 601 (2021) 196–208.
- [46] X. Ma, Y. Lv, J. Xu, Y. Liu, R. Zhang, Y. Zhu, A Strategy of Enhancing the Photoactivity of g-C₃N₄ Via Doping of Nonmetal Elements: A First-Principles Study, *J. Phys. Chem. C.* 116 (2012) 23485–23493.
- [47] R. Zhang, A. Zhang, Y. Yang, Y. Cao, F. Dong, Y. Zhou, Surface Modification to Control the Secondary Pollution of Photocatalytic Nitric Oxide Removal over Monolithic Protonated g-C₃N₄/Graphene Oxide Aerogel, *J. Hazard. Mater.* 397 (2020) 122822.
- [48] Q.-Q. Bi, J.-W. Wang, J.-X. Lv, J. Wang, W. Zhang, T.-B. Lu, Selective Photocatalytic CO₂ Reduction in Water by Electrostatic Assembly of CdS Nanocrystals with a Dinuclear Cobalt Catalyst, *ACS Catal.* 8 (2018) 11815–11821.
- [49] L. Zou, R. Sa, H. Zhong, H. Lv, X. Wang, R. Wang, Photoelectron Transfer Mediated by the Interfacial Electron Effects for Boosting Visible-Light-Driven CO₂ Reduction, *ACS Catal.* 12 (2022) 3550–3557.
- [50] M. Xu, X. Hu, S. Wang, J. Yu, D. Zhu, J. Wang, Photothermal Effect Promoting CO₂ Conversion over Composite Photocatalyst with High Graphene Content, *J. Catal.* 377 (2019) 652–661.
- [51] J. Wang, G. Zhang, P. Zhang, Graphene-Assisted Photothermal Effect on Promoting Catalytic Activity of Layered MnO₂ for Gaseous Formaldehyde Oxidation, *Appl. Catal. B-Environ.* 239 (2018) 77–85.
- [52] Z. Zhang, J.Y. Sun, X. Chen, G.Z. Wu, Z.G. Jin, D.G. Guo, L. Liu, The Synergistic Effect of Enhanced Photocatalytic Activity and Photothermal Effect of Oxygen-Deficient Ni/Reduced Graphene Oxide Nanocomposite for Rapid Disinfection under near-Infrared Irradiation, *J. Hazard. Mater.* 419 (2021) 126462.
- [53] S. Hu, J. Shi, B. Luo, C. Ai, D. Jing, Significantly Enhanced Photothermal Catalytic Hydrogen Evolution over Cu₂O-rGO/TiO₂ Composite with Full Spectrum Solar Light, *J. Colloid Interf. Sci.* 608 (2022) 2058–2065.
- [54] S. Luo, X. Ren, H. Lin, H. Song, J. Ye, Plasmonic Photothermal Catalysis for Solar-to-Fuel Conversion: Current Status and Prospects, *Chem. Sci.* 12 (2021) 5701–5719.
- [55] Q.L. Xu, D.K. Ma, S.B. Yang, Z.F. Tian, B. Cheng, J.J. Fan, Novel g-C₃N₄/g-C₃N₄ S-Scheme Isotype Heterojunction for Improved Photocatalytic Hydrogen Generation, *Appl. Surf. Sci.* 495 (2019) 143555.
- [56] L. Zhang, J. Zhang, H. Yu, J. Yu, Emerging S-Scheme Photocatalyst, *Adv. Mater.* 34 (2022) 2107668.
- [57] Q. Xu, S. Wageh, A.A. Al-Ghamdi, X. Li, Design Principle of S-Scheme Heterojunction Photocatalyst, *J. Mater. Sci. Technol.* 124 (2022) 171–173.
- [58] Z. Li, S. Ye, P. Qiu, X. Liao, Y. Yao, J. Zhang, Y. Jiang, S. Lu, An S-Scheme Alpha-Fe₂O₃/Cu₂O Photocatalyst for an Enhanced Primary Amine Oxidative Coupling Reaction under Visible Light, *Dalton T* 51 (2022) 10578–10586.
- [59] Y. Lu, X.F. Jia, Z.Y. Ma, Y. Li, S. Yue, X.F. Liu, J.Y. Zhang, W⁵⁺-W⁵⁺ Pair Induced Lspr of W₁₈O₄₉ to Sensitize ZnIn₂S₄ for Full-Spectrum Solar-Light-Driven Photocatalytic Hydrogen Evolution, *Adv. Funct. Mater.* 32 (2022) 2203638.
- [60] Y. Shang, C. Wang, C. Yan, F. Jing, M. Roostaeinia, Y. Wang, G. Chen, C. Lv, An Efficient and Multifunctional S-Scheme Heterojunction Photocatalyst Constructed by Tungsten Oxide and Graphitic Carbon Nitride: Design and Mechanism Study, *J. Colloid Interf. Sci.* 634 (2023) 195–208.
- [61] F. Xu, K. Meng, B. Zhu, H. Liu, J. Xu, J. Yu, Graphdiyne: a new photocatalytic CO₂ reduction cocatalyst, *Adv. Funct. Mater.* 29 (2019) 1904256.
- [62] J. Low, L. Zhang, B. Zhu, Z. Liu, J. Yu, TiO₂ photonic crystals with localized surface photothermal effect and enhanced photocatalytic CO₂ reduction activity, *ACS Sustain. Chem. Eng.* 6 (2018) 15653–15661.